High-Efficiency Single-Junction p-i-n GaAs Solar Cell on Roll-to-Roll Epi-ready Flexible Metal Foils for Low-Cost Photovoltaics

Devendra Khatiwada*[1,2,3], Carlos A. Favela*[1,2,3], Sicong Sun[1,2,3], Chuanze Zhang[1,2,3], Sahil Sharma[1,2,3], Monika Rathi[1,2,3], Pavel Dutta[1,2,3], Eduard Galstyan[1,2,3] , Alex Belianinov[4], Anton V Ievlev[4] , Sara Pouladi[1], Jae-Hyun Ryou[1,2,3], and Venkat Selvamanickam[1,2,3]

[1]Department of Mechanical Engineering, University of Houston, Houston, TX 77204, USA
[2] Advanced Manufacturing Institute, University of Houston, Houston, TX 77204, USA
[3] Texas Center for Superconductivity, University of Houston, Houston, TX 77204, USA
[4]Center of Nanophase Materials Sciences, Oak Ridge National Lab, TN 37830, USA

Abstract

In this paper, we demonstrate the fabrication and characterization of high-efficiency single-junction p-i-n GaAs solar cell on flexible epi-ready buffer on metal foils processed via roll-to-roll fabrication. Single-junction p-i-n GaAs solar cells were fabricated using metal-organic chemical vapor deposition (MOCVD). An efficiency greater than 13% was obtained at 1 sun, which is the highest reported efficiency on GaAs PV directly deposited on epi-ready metal buffers. The efficiency obtained exceeds our previous reported efficiency of 11% on single junction p-n solar cell structure. This is attributed to improvement in the quality of the junction, surface morphology, controlled diffusion of species within the active layers, and increase in absorption due to the optimized intrinsic layer thickness.

Introduction

The highest efficiency among all solar cells has been achieved in III-V semiconductor materials [1-4]. However, the cost of III-V materials is still high compared to other types of cells. Two basic approaches are being pursued for low cost III-V solar cells: Use of low-cost substrates (other than GaAs wafers) for growth of III-V semiconductor materials and epitaxial lift-off processes for re-use of GaAs wafer substrate. Non-GaAs substrates have been used for growth of III-V semiconductors, such as germanium (Ge), silicon (Si), or compositionally graded SiGe using the chemical vapor deposition (CVD) [5], molecular beam epitaxial (MBE) [6], and metal organic

chemical vapor deposition (MOCVD) techniques [7]. For Ge as substrate, the lattice mismatch between GaAs/Ge is just 0.07% at room temperature and results in compressive bi-axial stress in the growth plane which is compensated with an enlargement of the germanium (Ge) lattice in the direction of the growth [8, 9]. For Si as a substrate, the lattice mismatch between GaAs/Si of approximately 4% as well as differences in thermal expansion coefficients result in nucleation of a high density of threading dislocations greater than $10^8/cm^2$ [10]. Research has been done to reduce this threading dislocation using techniques such as graded Ge-Si buffer [11, 12]. However, GaAs solar cells fabricated on such substrates have not exhibited very high efficiency.

In another approach, an epitaxial lift off (ELO) technique for single-junction (1J) solar cells with sacrificial or release layer like aluminum arsenide (AlAs, AlGaAs, etc.) is employed to reuse the wafer [13-17]. Hydrofluoric (HF) acid is used as a solvent to etch the release layer [15, 18]. However, film cracking is induced as a consequence of repeated lift-off processes [19]. Today's world record efficiency of 29.3% for 1J GaAs via ELO was demonstrated by Alta Devices [20-22]. Research has been conducted to increase the ELO rate with hydrophilic solvents, such as acetone [23] and cleaning the GaAs substrate using a solution containing NH_4OH/ H_2O_2/H_2O (1:1:50) for reuse [24]. Despite these efforts, wafer reuse for ELO processing has a finite lifetime as several defective areas develop on the wafer that lead to a gradual decrease in efficiency. In addition, large scale production processes with ELO for low-cost manufacturing is questionable. Thus, there is a need for an alternative method to manufacture III-V solar cells at a low cost.

We have developed a novel epitaxial approach for growing low-cost and scalable GaAs solar cells on lightweight and robust substrates via a roll-to-roll process. The details of buffer and epitaxial growth are described elsewhere [25-27]. The previously reported solar cell structure grown and fabricated on flexible epi-ready metal tape were single junction p-n solar cells [28, 29]. The solar cell efficiency was mainly limited by absorption and leakage/recombination (arising from sidewalls, grain boundaries, defects etc.). The main type of defect was threading dislocations, of the order of $10^8\ cm^{-2}$, due to the 4% lattice mismatch between Ge and CeO_2 buffer layer [27, 28].

In efforts to address issues such as species diffusion, surface defects, and absorption, the device architecture was modified by inserting an intrinsic layer between the p-n junction to make a p-i-n structure. In the p-i-n structure, the electric field extends over a wider region while the

built-in potential is the same as the p-n, when using similar doping concentrations. This electric field drifts the photo-generated charge carriers in the intrinsic layer (towards the contact) in a way that increases the carrier diffusion length before recombination [30]. The intrinsic layer thickness also increases photo-absorption. This type of structure is common for amorphous silicon solar cells where the diffusion length is short [31] but has not been explored with GaAs solar cells in an epi-ready buffer.

P-i-n solar cells with different intrinsic layer thickness (250 nm,500 nm,1000nm,1500 nm and 2000 nm) were grown using MOCVD keeping the thickness and carrier concentration of all other layers unchanged. Imaging tools such as optical microscopy, Scanning electron microscopy (SEM), Atomic force microscopy (AFM), Helium ion microscopy (HIM) were utilized for surface characterization of fabricated p-n and p-i-n device films. P-n device films fabricated during same process were used to compare the p-i-n films. P-i-n solar cells with different intrinsic layer thickness were fabricated and characterized using illuminated and dark current-voltage (I-V) curves. The solar cell with optimized intrinsic thickness was processed further for cap layer removal and added an anti-reflection coating (ARC). Bulk characterization was performed using cross section Transmission electron microscopy (TEM) and SEM. Further, optical characterization of p-n and p-i-n solar cells was done using photo-response characteristics.

Metal-Organic Chemical Vapor Deposition of the p-i-n solar cell structure

III-V materials were grown in a custom-built MOCVD tool with dual chambers possessing wafer and roll-to-roll capabilities. Metal foils with sputtered epitaxial Ge template were used for solar cell device growth in a custom-built reactor with graphite susceptor designed to ensure uniform heating. Arsine (AsH_3) and trimethylgallium (TMGa) were used for the growth of GaAs. Trimethylindium (TMIn) and trimethylaluminum (TMAl) were used for growth of InGaAs and AlGaAs, respectively. Dimethylzinc (DMZn) and Silane (SiH_4) were used as p-type and n-type dopants, respectively. Research purity hydrogen (H_2; 5N9) gas was further purified to 9N9 levels by a palladium (Pd) cell purifier and used as the carrier gas for MOCVD growth. In preparation for the device growth runs, control runs were performed to ensure correct doping concentration as confirmed via Hall measurement using a Van der Pauw configuration at room temperature with an HMS-5000 Ecopia system. A plasma-assisted (PAG) layer of ~200nm GaAs was initially grown at 550^{o}C and a chamber pressure of 1 Torr. The succeeding layers were grown at a chamber

pressure of 70 Torr. After the growth of the PAG layer, an undoped 1.8µm-thick GaAs layer was grown to prevent diffusion of Ge atoms to the active device layers [29]. Two sets of superlattice structure (SLS) comprised of 5nm thick (10nm total) GaAs/InGaAs alternating layers were grown for a total of 30 periods per SLS, with 1.2 µm of undoped GaAs serving as a spacer between sets of SLS. The purpose of these SLS is to reduce defect density and serve as a Ge diffusion barrier. GaAs and InGaAs layers were grown at 650°C. Another 1.2 µm thick undoped GaAs was grown on the 2nd set of SLS to further reduce the defect density. Next, a 1.4 µm thick highly-doped p^{++} GaAs layer with a bulk concentration (BC) of $5.0\times10^{19}cm^{-3}$ was grown to serve as a current-spreading layer for lateral contacts. A ~33nm p^{++} ($1.0\times10^{19}cm^{-3}$) back-surface field (BSF) AlGaAs layer was grown, followed by a 50nm p-GaAs layer ($1.0\times10^{18}cm^{-3}$) and an intrinsic GaAs layer of thickness varying from ~250-2000nm (250nm, 500nm, 1000nm, 1500nm and 2000nm). The growth of the intrinsic GaAs was followed by ~67nm of n^{+}-type GaAs ($1.0\times10^{17}cm^{-3}$) emitter, ~30nm of n^{++} ($1.0\times10^{19}cm^{-3}$) AlGaAs window layer and finally a ~33nm n^{++} GaAs ($1.0\times10^{19}cm^{-3}$) cap layer. The thickness variation in each layer is in the range of ±3nm.

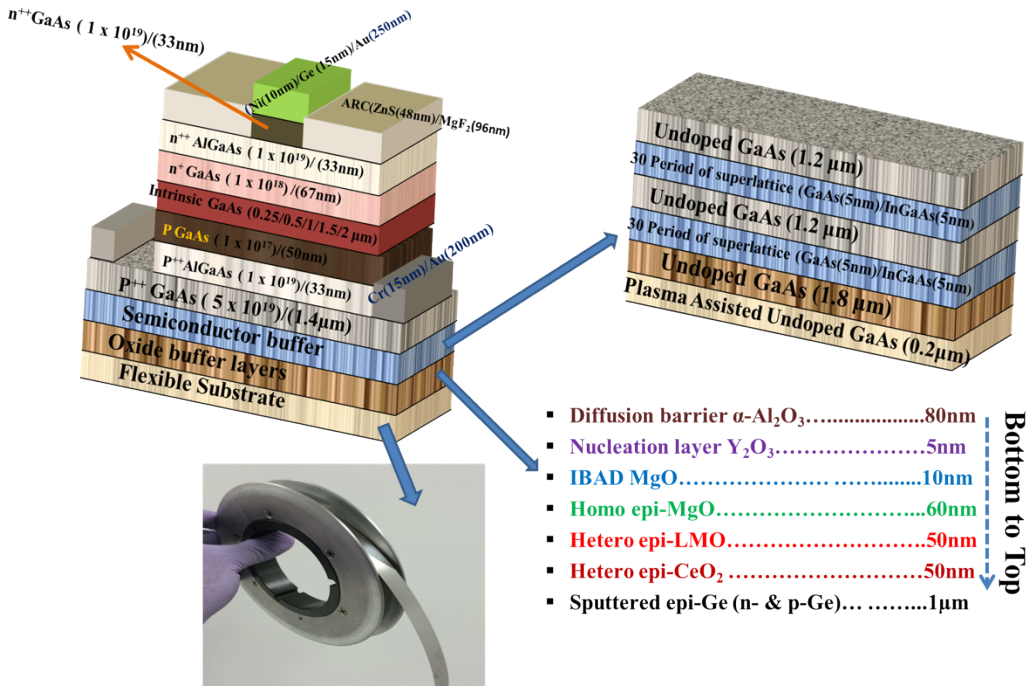

Figure 1. Schematic of 1J p-i-n solar cell and buffer layer on flexible metal tape.

A detailed image of the p-i-n single junction GaAs solar cell structure is shown in figure 1. The doping concentration and fabrication condition for all layers in the p-i-n structure were kept the same as that of p-n solar cells. In the case of the p-i-n structure, the intrinsic layer thickness was varied to achieve maximum current generation.

Optical characterization of p-n and p-i-n solar cell device films

The visual appearance of both p-n and p-i-n devices was specular and shiny when retrieved from the sample chamber. However, when examined under an optical microscope, their morphology was very different, with substantial more particles in p-n device samples. Optical, SEM and AFM images were obtained to determine the nature of the particles on the surface of the p-n GaAs device film, and were compared with the p-i-n versions as shown in figure 2 and 4, respectively. The optical images reveal the presence of random-sized black-spotted features (defects) resembling pits and particles. The p-n device samples had a higher concentration of these features. These features were estimated to cover 8% of the 110μm by 80μm image area (>7 images per sample). In comparison, the features found in the p-i-n sample were present in <1% of the same image areas. SEM of the p-n device sample reveal smaller features (~1 μm^2) present in the sample not seen in the optical images. In contrast, the morphology of the p-i-n sample is relatively clean. To determine whether the features are pits or particles, high-resolution AFM imaging was conducted. The average root-mean-square roughness obtained from a AFM surface topography scan of an area of 40 μm × 40 μm taken over different areas of the sample is 180 nm. A 3D image from a scan over a 10 μm × 10 μm area shows a pit with a depth of approximately ~750 nm. This confirms the features to be pits and suggests that many were formed on the p-n solar cell surfaces. These pits are likely the center for diffusion and a reason for the high leakage observed in p-n solar cells. However, the exact pit widths and the features inside the pits are still unknown.

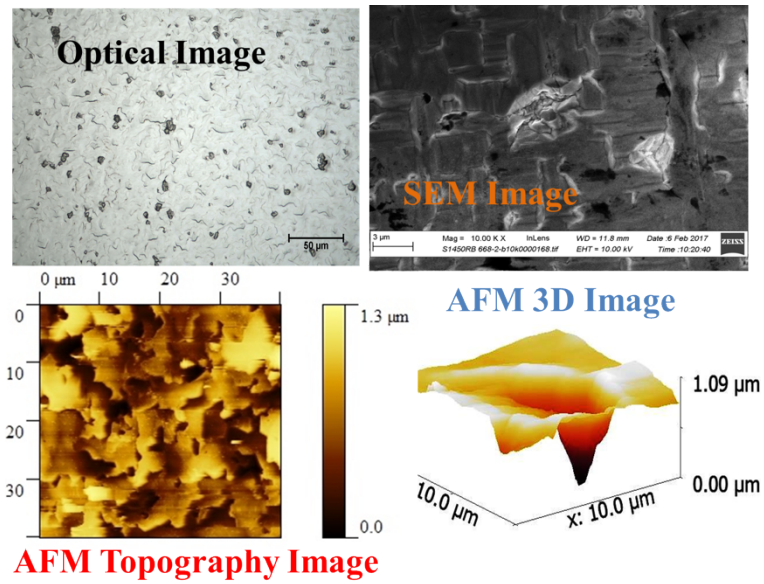

Figure 2. Optical, SEM and AFM images of p-n films.

Helium ion microscopy was used to image the surface of p-n solar cell films to better understand the widths of the pits as well as their features. Helium ion microscopy is a type of Field Ion Microscopy (FIM) that uses a Gaseous Field Ionization Source (GFIS) gun with helium gas at the vicinity [30]. It typically operates between 20 keV to 45 keV and can produce a helium beam current in the range of 10^{-14} to 10^{-11} A. Changing the background pressure of the imaging gas, the beam current can be modulated [31]. For beam energy in the given range (20-45 keV), the wavelength of the helium ion is several hundred times shorter than that of electron beams of the same energy (used in SEM), generating high momentum to reduce diffraction. The depth-of-field for HIM is thus 10x to 20x larger than that of SEM [32]. ORION NF equipment (at Oak Ridge National Laboratory) that produces a beam (convergence angle of 0.5 mrad) with a probe size of 0.4 nm and a beam current in picoamperes (pA)was used for our experiment. For imaging the p-n solar cell surfaces at a working distance of 17.12 mm, a beam current of 0.589 pA was used for all sizes of images.

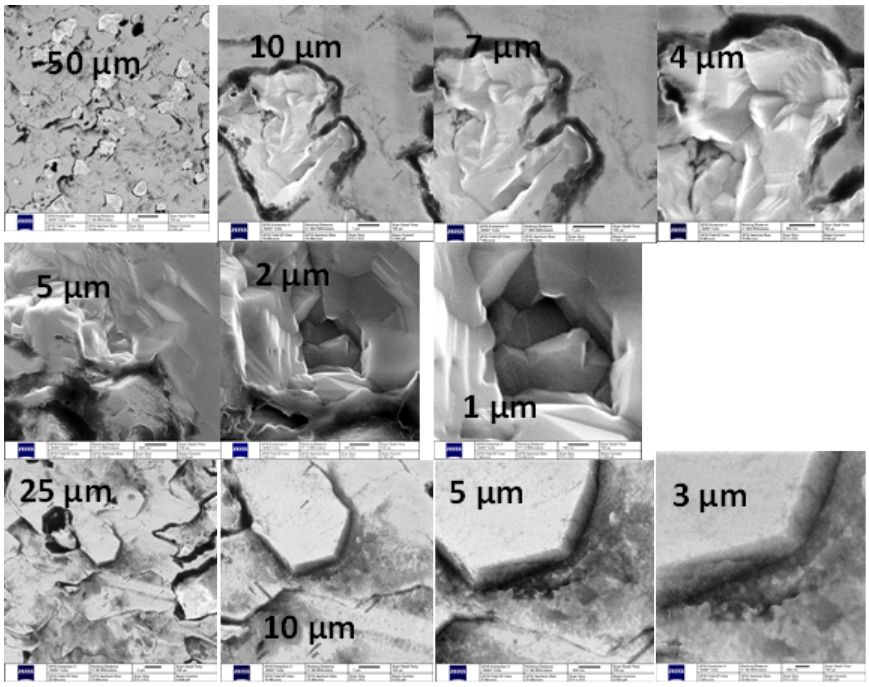

Figure 3. HIM images of p-n film surfaces.

Figure 3 shows the HIM images of p-n solar cell surfaces at different locations. In the first row of images in figure 3, the low magnification image (50 µm) shows a concentration of spots on the surface. The high magnification images clearly show that the surface spots are pits. The 1 µm image in the 2nd row is a clear evidence for the formation of such pits. The width of those pits varied from approximately 400 nm to 650 nm. This high concentration of pits in the p-n solar cell led to high leakage, low current and lower open circuit voltage. When metal contacts are deposited during the fabrication process, the pit's area will short the device. The third row of images supports the AFM observation of roughness on the surface of the p-n GaAs film. The growth mode appears to be layer-by-layer with some localized step features leading to a rougher film.

The surface morphology of the grown p-i-n solar cells with different intrinsic thicknesses were of the same nature as observed by optical, SEM and AFM imaging. Data from a sample with an intrinsic layer thickness of 1000 nm is shown in figure 4. The optical and SEM images show a clean surface with a very low concentration of black spots. The average root-mean-square roughness obtained from a scan area of 40 µm × 40 µm was 50 nm. The 3D image scan of the 10 µm × 10 µm area clearly shows that the surface of the film is clean with no pits within that scan range. This is a clear evidence of a cleaner surface in the p-i-n film compared to the p-n film. Still, few pits and some particles were revealed in a larger-area scan.

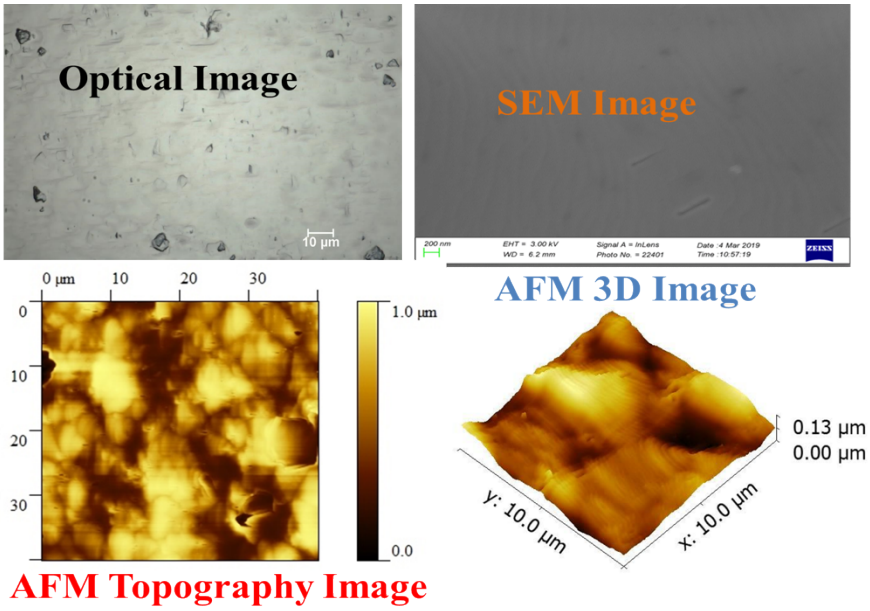

Figure 4. Optical, SEM and AFM images of p-i-n film.

HIM analysis of the p-i-n film is shown in figure 5. HIM surface imaging of p-i-n surfaces was performed at the same working distance and beam current as applied for the p-n sample. The scan sizes between 250 µm and 1.3 µm at different locations supports the observation from SEM and AFM that the concentration of pits is greatly reduced. The growth mode appears to be layer-by-layer.

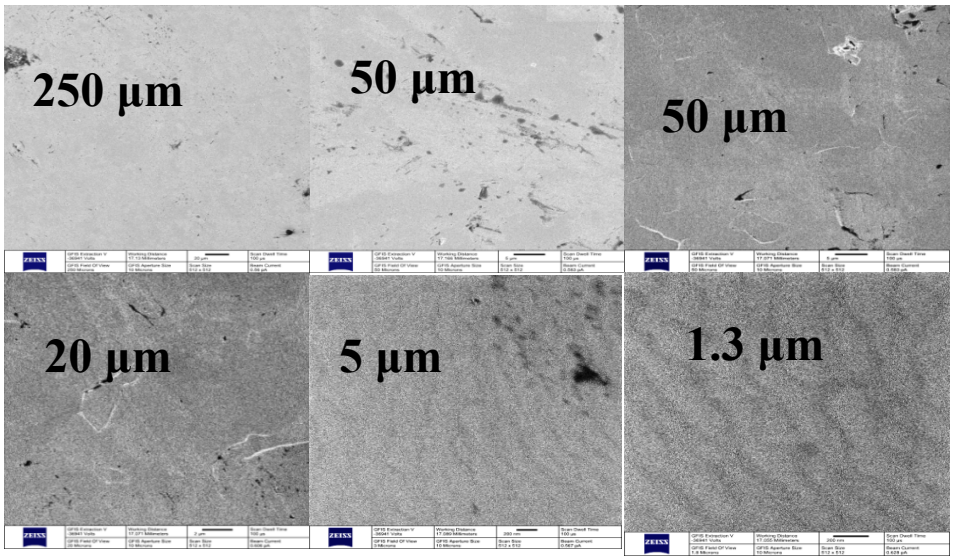

Figure 5. HIM images of p-i-n film surfaces.

Thus, the p-i-n films showed a smoother morphology than p-n films. As mentioned above, surface analyses of the p-i-n films of different intrinsic layer thicknesses showed nearly identical morphologies. These p-i-n films with different intrinsic layer thicknesses were then fabricated as completed devices.

Fabrication and characterization of single-junction p-i-n solar cells

The fabrication process for the p-i-n solar cells was the same as for the p-n solar cells described in our previous work [28] except for the etching process for the different thickness of the intrinsic layers. The flexible samples were pasted on a wafer and processed via lithography and contact deposition. The ohmic contact nature of the fabricated samples was tested using Transmission Line Method (TLM). The TLM characterization of the p-n solar cell is shown in supplementary information. The specific contact resistivities of n- and p-type contacts were 1.5×10^{-4} Ωcm^2 and 9×10^{-5} Ωcm^2, respectively. Comparing with the p-n device, a lower contact resistance (12Ω in p-n and 1.35Ω in p-i-n) and sheet resistance (360Ω/sq in p-n and 31.3Ω/sq in p-i-n) were observed for the p-i-n device film. This is attributed to a smooth p-i-n surface with negligible surface pits and particles compared to the p-n surface.

After measuring the TLM, the solar cell efficiencies were measured from J-V curves. An NREL-calibrated Oriel 200 series solar simulator at 1 sun was used to obtain illuminated J-V behavior. Figure 6 shows the illuminated curve for p-i-n solar cells with intrinsic layer thicknesses of 250 nm, 500 nm, 1000 nm, 1500 nm and 2000 nm. The parameters obtained from the J-V curve is shown in table 1. All devices were measured after the initial stage of device fabrication.

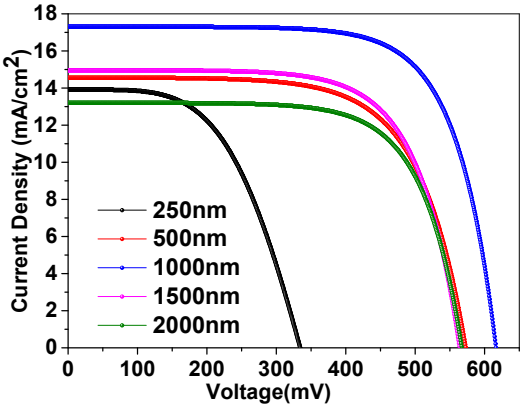

Figure 6. Illuminated J-V characteristics of the fabricated p-i-n GaAs solar cells with different intrinsic layer thicknesses.

Table 1. V_{OC}, J_{SC}, FF and η of p-i-n solar cells with different intrinsic layer thicknesses

Intrinsic layer thickness (nm)	V_{OC} (mV)	J_{SC} (mA/cm^2)	Fill Factor (%)	Efficiency (%)
250	334	13.8	0.51	2.8
500	568	14.7	0.67	5.7
1000	615	17.4	0.71	7.6
1500	564	15	0.63	5.6
2000	567	13.2	0.66	5.0

As observed from the above J-V curves in figure 7 and table 1, the V_{OC}, J_{SC}, FF and η values all followed certain trend as the thickness of the intrinsic layer was varied. The best result is observed for the intrinsic layer thickness of 1000 nm. Figure 8 shows the variation of V_{OC}, J_{SC} and FF values for different intrinsic layer thicknesses.

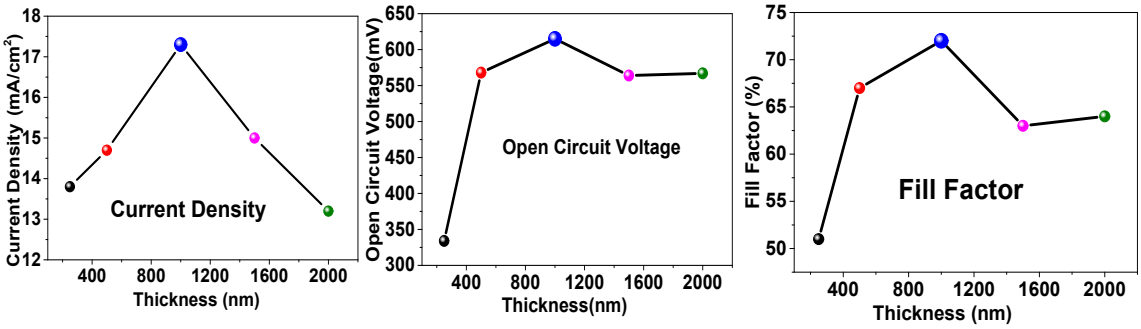

Figure 7. Variation of J_{SC}, V_{OC} and FF of p-i-n cells with different intrinsic layer thicknesses.

As observed from figure 7, the J_{SC} increased as the intrinsic layer thickness increased from 250 nm; it reached a maximum value at 1000 nm and then decreased for thicker intrinsic layers (1500 and 2000nm, respectively). As explained previously, the lower J_{SC} for the thinner base is due to insufficient absorption of light. As the thickness increases, the absorption increases initially then decreases for thicker intrinsic layers due to increased defects (low carrier lifetimes in thicker base limit the diffusion length). The open circuit voltage and fill factor is maximum for 1000 nm

and minimum for 250 nm intrinsic thicknesses. This effect can be explained from dark I-V characteristics for different intrinsic layer thicknesses.

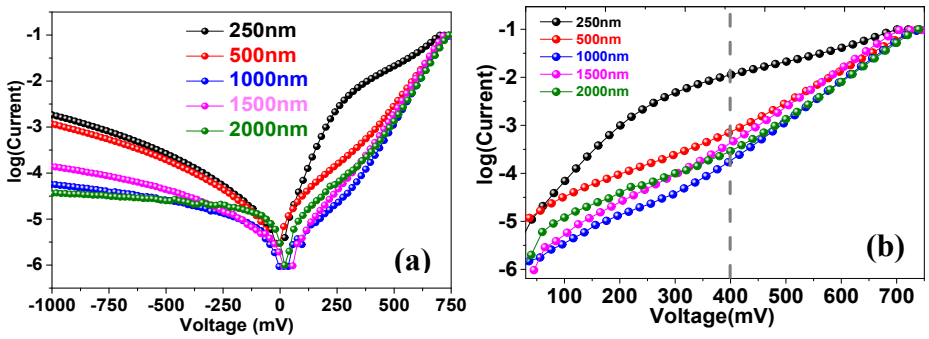

Figure 8. Dark I-V characteristics of the fabricated p-i-n GaAs solar cell.

Figure 8 (a) shows the log-scale plot of the dark I-V curves of p-i-n cells with different intrinsic layer thicknesses, and 8 (b) shows the same plot with the component of forward-biased dark current. The dark curve in the forward-biased case comprises of two regions (i.e., the lower voltage and higher voltage regions) distinguished by the indicated vertical line. The performance can be approximated by two diodes in parallel with parasitic resistance R_s and can be expressed as,

$$J_{dark}(V) = J_{01}\left[\exp\left\{q\left(\frac{V - J_{dark}R_s}{kT}\right)\right\} - 1\right] - J_{02}\left[\exp\left\{q\left(\frac{V - J_{dark}R_s}{2kT}\right)\right\} - 1\right]$$

where J_{01} and J_{02} are the saturation current densities (recombination component) at higher and lower voltage regions, respectively. T is the operating temperature (25 °C for standard solar cell test condition), q is electronic charge, and k is Boltzmann's constant. In the low-voltage region, the second diode with the 2kT component dominates, and in the high-voltage region, the first diode with the 1kT component dominates. The low-voltage region in the forward-bias case gives information on the recombination at the space charge region (SCR), and the high-voltage region gives the information on recombination at the quasi-neutral region (QNR). The leakage current calculated from the dark I-V plot for different intrinsic layer thicknesses is tabulated in table 2 below.

Table 2. Leakage current (I_O) of p-i-n solar cells with different intrinsic layer thicknesses.

Intrinsic layer thickness (nm)	250	500	1000	1500	2000

Leakage current (I_O) (mA)	4×10^{-3}	2×10^{-3}	8×10^{-5}	1×10^{-4}	6×10^{-5}

From the above table 2, it is seen that a leakage current in the range of 10^{-5} mA was obtained for a cell with an intrinsic layer thickness of 1000 nm, whereas it is two orders of magnitude higher for a cell with an intrinsic layer thickness less than 1000nm. For a cell with an intrinsic layer thickness of 1500 nm, the leakage current increases by an order of magnitude compared to the 1000 nm cell. The leakage current decreases in the cell with an intrinsic layer thickness of 2000 nm. To understand the trend in the leakage current due to the intrinsic layer thickness, the dark current-voltage curve was fitted with a double-diode model, as explained in the above equation. The double-diode fit at the forward-voltage region for an intermediate intrinsic layer thickness of 1000 nm and thickness of 250 nm is shown in figures 10 (a) and (b), respectively.

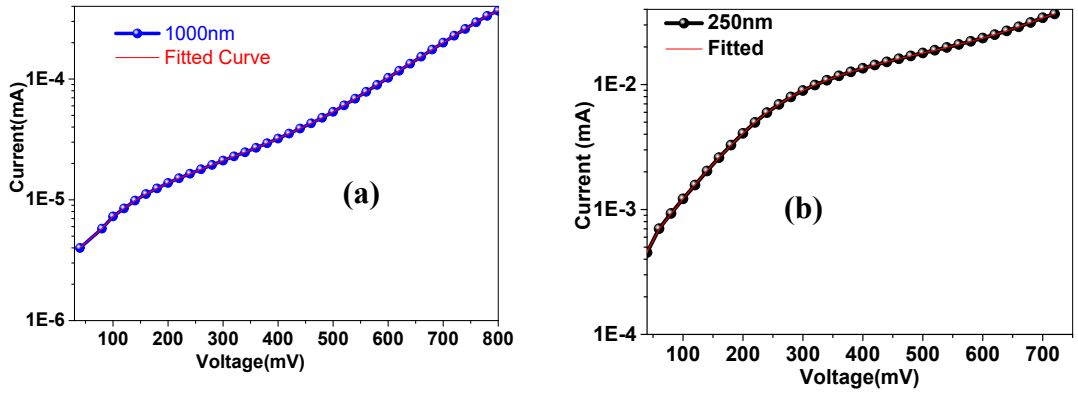

Figure 9. Forward-bias component of dark curve fit.

Table 3. Saturation current density from double-diode fitting.

Intrinsic Layer thickness (nm)	250	500	1000	1500	2000
J_{o1} (A/cm^2)	2.3×10^{-9}	2.6×10^{-9}	3.9×10^{-10}	5.8×10^{-9}	2.5×10^{-9}
J_{o2} (A/cm^2)	6.3×10^{-7}	4.4×10^{-8}	3.1×10^{-9}	1.42×10^{-8}	1.1×10^{-8}

Table 3 shows the extracted saturation current density obtained from the fit for different intrinsic layer thicknesses. From the double-diode fit in figure 9(a), the extracted values of J_{o1} and J_{o2} for an intermediate intrinsic layer thickness of 1000 nm are 3.9×10^{-10} A/cm^2 and 3.1×10^{-9}

A/cm^2, respectively. As observed from the leakage current, for an intrinsic layer of thickness 250 nm, the leakage current is two orders of magnitude higher than that of the cell with 1000 nm intrinsic layer thickness. This can be explained from the above-mentioned fact (illuminated J-V showing lower current) that the field generated within the intrinsic layer of thickness 250 nm is not sufficient to deplete the photo-generated charge carriers generated. So, these charge carriers recombine before collection, causing higher leakage. The forward-biased region of the dark curve, as shown in figure 9 (b), also supports the higher recombination mechanism with the intrinsic layer thickness of 250 nm. From the double-diode fit in figure 10 (b), the extracted value of J_{o1} and J_{o2} values for a thinner intrinsic layer of 250 nm are 2.3×10^{-9} A/cm^2 and 6.3×10^{-7} A/cm^2, respectively. The value of J_{o1} is one order of magnitude higher, and the value of J_{o2} is two orders of magnitude higher than that for intrinsic layer thickness of 1000 nm. This clearly shows that the recombination in the space-charge region and the quasi-neutral region is higher for an intrinsic layer thickness of 250 nm.

We observed a similar trend for an intrinsic layer with a thickness of 500 nm. The J_{o1} and J_{o2} values were $2.6\times10^{-9}A/cm^2$ and $4.4\times10^{-8}A/cm^2$, respectively. The value of J_{o1} is thus comparable to the cell of 250 nm thick intrinsic layer, whereas the value of J_{o2} is one order of magnitude higher than the 1000-nm thick layer cell and one order of magnitude lower than the 250 nm thick layer cell. Thus, the recombination in SCR for 500 nm thick layer cell is higher than that of the 1000 nm thick layer cell but lower than that with the 250 nm thick layer cell. This is supported by the fact that the leakage current follows the trend.

As the thickness of the intrinsic layer increases from 1000 nm to 1500nm, the charged defects increase, which reduces the net electric field in the region and increases recombination. This fact is also supported by higher values of J_{01} ($5.8\times10^{-9}A/cm^2$) and J_{02} ($1.42\times10^{-8}A/cm^2$) for the 1500 nm thick layer cell compared to the 1000 nm thick layer cell, resulting in higher leakage. When the intrinsic layer thickness increases to 2000 nm, the net electric field increases, which is higher than in the cell with intermediate layer thickness. However, recombination due to the charged defects increases. Due to this trade off, a lower leakage was observed but with reduced current in the cell with an intrinsic layer thickness of 2000 nm. Careful comparison of the low-voltage region on the forward-biased side shows that the value of J_{02} is higher (1.1×10^{-8} mA/cm^2)

for the 2000-nm-thick intrinsic layer compared to the 1000 nm thick layer (3.1×10^{-9} mA/cm^2), indicating higher recombination occurring at the space-charge region.

Therefore, the optimal thickness for the intrinsic layer is 1000 nm, since the cell with this thickness exhibited the lowest leakage current and high values of $V_{OC,}$ $J_{SC,}$ FF and η. To further enhance the device efficiency, p-i-n solar cells with this intermediate thickness (1000nm) of the intrinsic layer underwent further steps of device fabrication (cap layer removal/passivation and ARC).

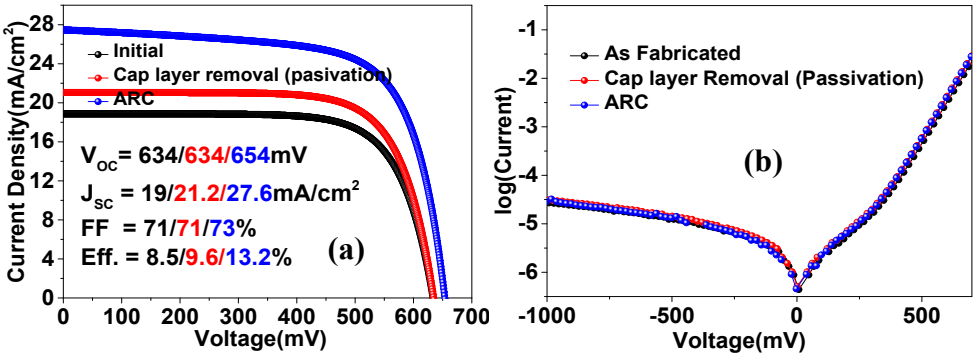

Figure 10. (a) Illuminated and (b) dark current-voltage characteristic of a p-i-n solar cell with a 1000-nm intrinsic layer at each step of device fabrication.

Figure 10 shows the illuminated J-V characteristic for a fabricated p-i-n solar cell with an intrinsic layer thickness of 1000 nm at three different stages of device fabrication. For cap layer removal, a 1:1 mixture of citric acid ($C_6H_8O_7$) and hydrogen peroxide (H_2O_2) at room temperature was used. After cap layer removal, the J_{SC} of solar cell increased from 19mA/cm^2 to 21.2mA/cm^2, whereas the leakage current remained the same. To further enhance the current density by minimizing the surface reflection, ARC was deposited. Zinc sulfide (48 nm) and magnesium fluoride (96 nm) were used as ARC for consistency with p-n solar cells. The short circuit current density further increased after ARC coating from 21.2 to 27.6 mA/cm^2, keeping the leakage current constant. Table 4 provides details regarding the extracted parameters for solar cells at three different stages of device fabrication. The fill factor of the solar cell at different stages of device fabrication remained almost constant. The leakage current also remained almost constant with a value of 5×10^{-5}mA.

Table 4. I_o, V_{OC}, J_{SC}, FF and η of solar cells at the initial stage of fabrication, after cap layer removal and after ARC application.

Stage of Device Fabrication	V_{OC} (mV)	J_{SC} (mA/cm^2)	Fill Factor (%)	Efficiency (%)	Leakage current (I_O) (mA)
As Fabricated	633	19.2	0.71	8.5	5×10^{-5}
Cap Layer Removed	633	21.2	0.71	9.6	5×10^{-5}
ARC Applied	653	27.6	0.73	13.2	5×10^{-5}

An efficiency of 13.2% was obtained for p-i-n solar cells with an intrinsic thickness of 1000 nm. To better understand the p-i-n stack, a cross-sectional TEM analysis was performed. We used a p-i-n solar cell device with an optimized intrinsic layer thickness of 1000 nm. The results were compared from analysis of a p-n sample.

Transmission electron microscopy analysis of p-i-n and p-n solar cell stacks

Samples for cross-sectional TEM were prepared using FEI 235 dual beam focused ion beam system. Transmission electron cross-sectional imaging was carried out using a JEOL JEM 2000FX microscope at 200 keV. Figure 11 shows the complete architecture of p-n and p-i-n samples starting from the germanium buffer. The multilayered architecture consists of germanium, semiconductor buffer comprising of 2-µm undoped GaAs/ 30period of superlattice (GaAs, 5nm/ InGaAs, 5nm)/ 1.2µm of undoped GaAs/ 30period of superlattice/ 1.2µm of undoped GaAs, and a single-junction solar cell stack with p-n and p-i-n solar cell structures (active layer). A high density of defects was observed in the germanium film, starting from the Cerium Oxide (CeO_2) / Germanium (Ge) interface, which is due to a 4.2% lattice mismatch between the two layers as previously discussed [26, 33, 34]. The cross section analyzed by TEM shows that the incorporation of the strained layer superlattice reduces the density of threading dislocation on both the p-n and p-i-n structures. This commonly-used technique including a strained layer superlattice is capable of bending over the dislocation lines, creating barriers against the dislocation [35, 36]. As observed from the image, many dislocations are terminated or reflected at the superlattice, which result in a low dislocation density in the upper part of film above the superlattice. The active region comparison between the p-n and p-i-n shows that the active region of the p-i-n GaAs is relatively clean with fewer defects.

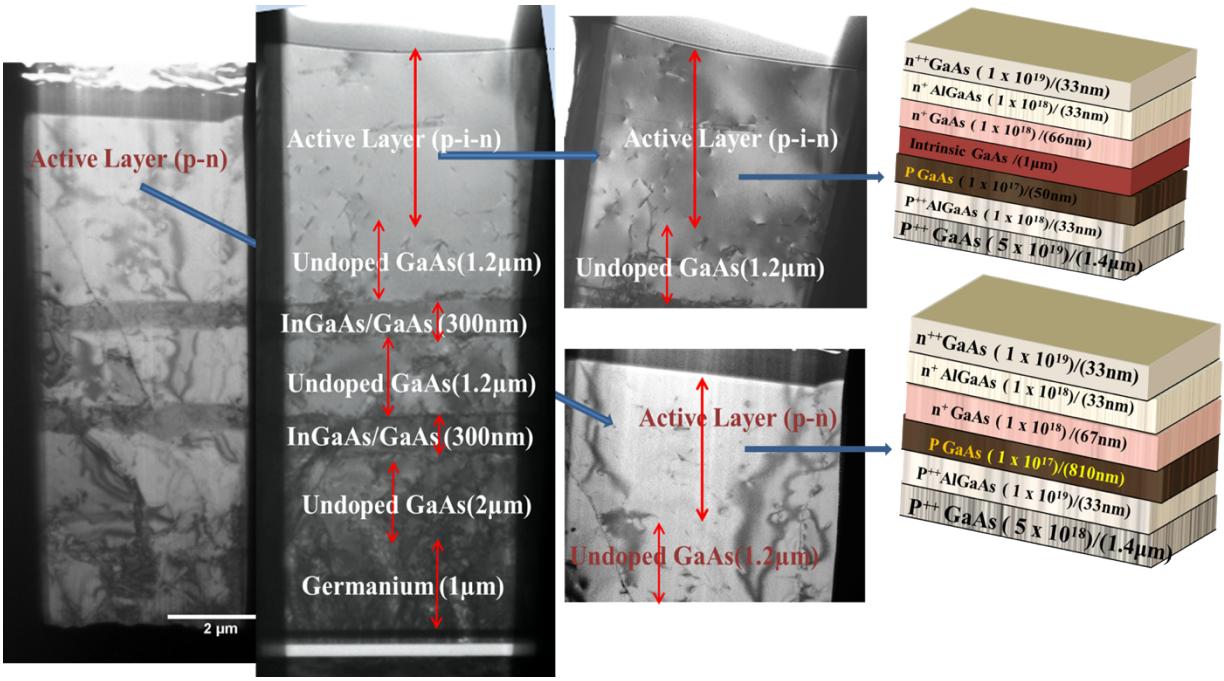

Figure 11. TEM analysis of cross-sections of the p-n and p-i-n devices.

The above TEM analysis showed that cleaner surfaces with less defects are obtained via introduction of an intrinsic layer in p-i-n type solar cell structures in comparison to p-n. The dislocations observed in the p-n and p-i-n structures act as a potential diffusion path for the dopants. To analyze the elemental species and diffusion of dopants, if any, time-of-flight secondary ion mass spectroscopy (TOF SIMS) was conducted on both p-n and p-i-n samples.

Time-of-Flight Secondary Ion Mass Spectrometry analysis for p-i-n and p-n films

Time-of-flight secondary ion mass spectrometry (TOF-SIMS) was used to determine elemental species present in p-n and p-i-n device films. TOF-SIMS measurements in this study were performed using TOF.SIMS.5 NSC instrument (ION.TOF Gmb). Bi_3^+ liquid metal ion gun (energy 30 keV, current 30 nA and spot size 5 µm) was used as a primary source scanned over an area of 100 × 100 µm for extraction of the secondary analyte ions. An additional Cs^+ ion gun (energy 1 keV, current 75 nA and spot size ~25 µm) scanned over 300 × 300 µm was used as a sputter source for depth profiling. A time-of-flight mass analyzer was operated in positive ion detection mode and enabled mass resolution m/Δm=2,000 - 10,000. Measurements were performed in a non-interlaced mode, where each analysis scan with Bi_3^+ were followed by 5 s of the sputtering with Cs^+. Chemical data was further averaged in the x-y direction and represented

as 1D depth profiles for different chemical elements (e.g., Ga^+, Al^+, As^+). Depth calibration was performed using know structure of the sample (thickness of different layers) and assuming constant sputter rate within chemically uniform layers.

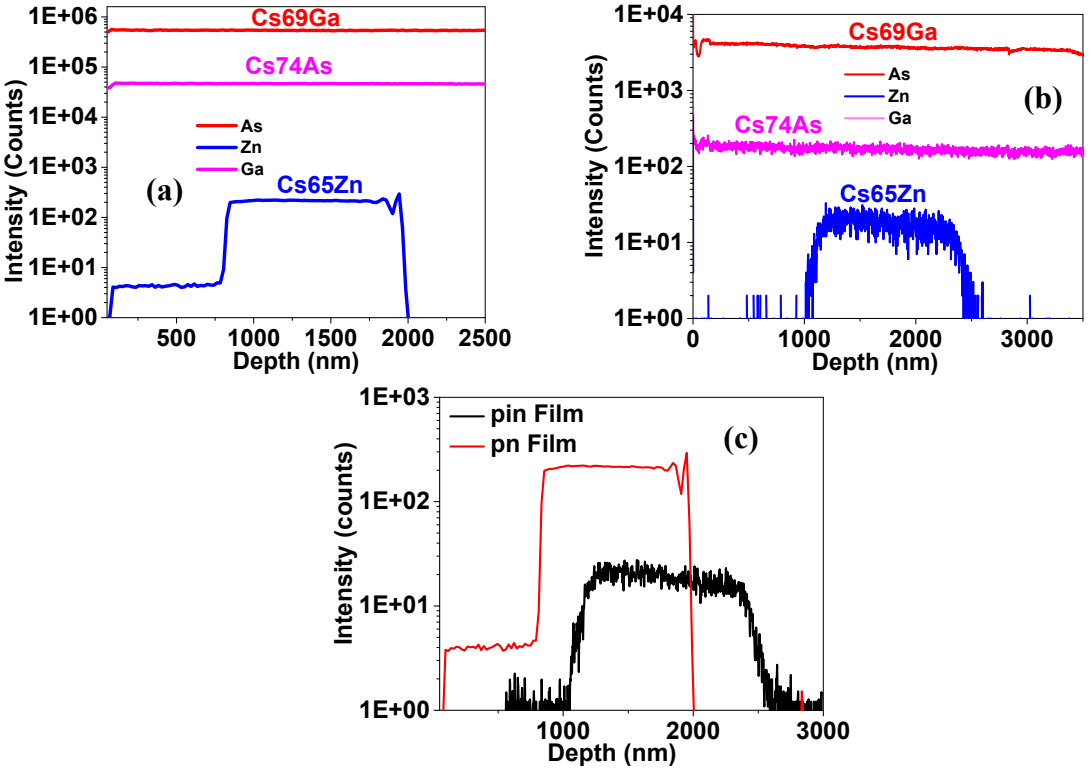

Figure 12. Depth profile analysis of elements in p-n (a) and p-i-n (b) films. Comparison of Zn profiles in p-n and p-i-n films are shown in (c)

Figure 12 (a) shows the depth profile of gallium, arsine and zinc down to 2500 nm in p-n films. Gallium and arsine appear throughout the etch depth, whereas the zinc distribution starts at around 80 nm (at n^+ GaAs) and stays constant to 800 nm (at p GaAs/base), after which its intensity increases to a depth of 850 nm (at p GaAs/base). From depths of 850 nm to 1970 nm (at p^{++} GaAs), the Zn level remains constant and then the intensity decreases. This shows that a small amount of zinc is diffused in the emitter region from approximately 60 nm to 133 nm of the depth. Thus, this disturbs the p-n junction region (i.e., the depletion width decreases with decreases in the effective electric field) leading to lower V_{OC}. The error margin of depth determination is ±5 nm.

Figure 12 (b) shows the depth profiles of a p-i-n device film. The gallium and arsine distribution are similar to the p-n cell. The zinc distribution starts at depth of 1080 nm, which is almost the depth of the intrinsic layer. This demonstrates absence of the zinc diffusion above or

into the intrinsic layer, which means that this layer stops the diffusion process. The zinc concentration increases from 1080 nm (approximately after intrinsic layer) and saturates after 1130 nm (after p-GaAs) up to 2400 nm. Figure 12 (c) shows the comparison between the zinc distribution depth profiles in p-n and p-i-n devices. It explains why leakage current in the case of a p-n junction (~10^{-3}mA) is higher than that of a p-i-n junction (~10^{-5}mA). In the case of a p-n junction, due to the diffusion of the p-dopant (zinc), the effective depletion width (electric field) decreases, which increases the tunneling current near the depletion layer and causes more leakage. With an optimized thickness of the intrinsic layer, the diffusion of species completely stops and leads to an overall improvement in device efficiency. Further, to understand the absorption difference in the p-n and p-i-n devices, the photoelectric response was analyzed.

Photoelectric response of p-n and p-i-n solar cells

The photoelectric response of p-n and p-i-n solar cells under zero bias and up to the wavelength of 700 nm is shown in figure 13. In p-n solar cells, the photocurrent increases with wavelength and reaches its maximum at a wavelength of 550 nm. Then, it remains constant until 600 nm and rapidly decreases. In p-i-n solar cells, the photocurrent increases with wavelength and reaches its maximum at 660 nm. Then, it remains constant until 700 nm. The maximum photo-response is found to increase to longer wavelengths in the case of the p-i-n solar cell structure. The current response for both p-n and p-i-n structures at the lower-wavelength region is due to insufficient extraction of carriers in window and emitter layers.

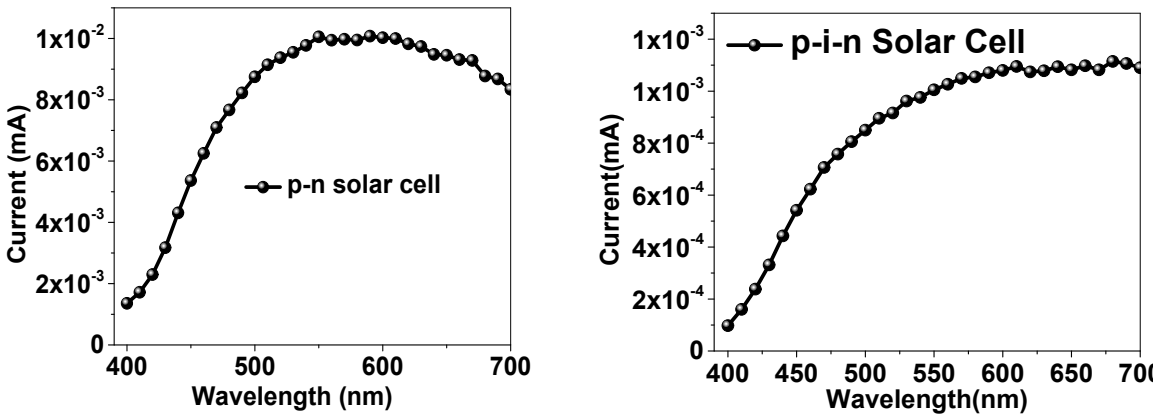

Figure 13. Photoelectric response for p-n and p-i-n solar cells.

The constant photo response at longer wavelengths is attributed to the longer carrier lifetimes in p-i-n solar cells compared to p-n solar cells. This point is also supported by the fact that the current density for p-i-n solar cells is higher than that of p-n solar cells. Thus, the overall efficiency of p-i-n solar cells exceeds the efficiency of p-n solar cells.

Conclusion:

In order to improve the device efficiency of single-junction GaAs solar cells on flexible metal substrate, p-i-n structures comprising different intrinsic layer thicknesses (250 nm, 500 nm, 1000 mm, 1500 nm and 2000 nm) were grown. Data obtained from the J-V characteristic showed that the cell with an intrinsic layer of thickness 1000 nm had the least leakage current with the highest values of V_{oc} and J_{sc} compared to cells with other intrinsic thicknesses. The solar cell device with an intrinsic layer of thickness of 1000 nm was further processed (i.e., cap layer removal and ARC) to achieve an efficiency of 13.2%. A comparison between the surface morphologies of p-n and p-i-n solar cell devices using AFM, SEM and HIM revealed that p-i-n solar cells were mostly free of pits and particles. SIMS analysis revealed diffusion of zinc in the p-n film, and that the intrinsic layer was effective in stopping diffusion in the p-i-n film. This improved the leakage current in the p-i-n film. The optical response of the p-i-n solar cell device with an intrinsic layer of thickness 1000 nm showed less recombination and absorption at longer wavelengths compared to the response of its p-n counterpart. In conclusion, p-i-n solar cells with an optimized intrinsic layer thickness resulted in better morphology, device results, and showed a better pathway to improve solar cell efficiency than p-n solar cells.

Acknowledgement:

This work is partially funded by the U.S. Department of Energy SunShot Initiative award DE-EE0006711. The part the research (HIM and ToF-SIMS) was conducted at the Center for Nanophase Materials Sciences, which is a DOE Office of Science User Facility, and using instrumentation within ORNL's Materials Characterization Core provided by UT-Battelle, LLC under Contract No. DE-AC05-00OR22725 with the U.S. Department of Energy.

Author Contributions:

D. Khatiwada and C. Favela equally contributed to the work. D. Khatiwada and C. Favela conceived, assembled, analyzed and co-wrote the manuscript. D. Khatiwada fabricated the devices and C. Favela conducted the MOCVD growth. S. Sun, and C.Zhang, assisted and contributed in engineering the underlying buffer structure which helped to grow single-crystalline-like Ge thin films of metal substrates. V. Selvamanickam provided expert guidance, insightful suggestions and project funding. All other authors discussed and commented on the manuscript.

References

1. Dimroth, F., *High-efficiency solar cells from III-V compound semiconductors.* physica status solidi c, 2006. **3**(3): p. 373-379.
2. King, R., et al., *40% efficient metamorphic GaInP/ GaInAs/ Ge multijunction solar cells.* Applied physics letters, 2007. **90**(18): p. 183516.
3. Dimroth, F., et al., *Wafer bonded four-junction GaInP/GaAs//GaInAsP/GaInAs concentrator solar cells with 44.7% efficiency.* Progress in Photovoltaics: Research and Applications, 2014. **22**(3): p. 277-282.
4. Yamaguchi, M., *III–V compound multi-junction solar cells: present and future.* Solar energy materials and solar cells, 2003. **75**(1-2): p. 261-269.
5. Fan, J.C., C.O. Bozler, and B.J. Palm, *Calculated and measured efficiencies of thin-film shallow-homojunction GaAs solar cells on Ge substrates.* Applied Physics Letters, 1979. **35**(11): p. 875-878.
6. Miller, D. and J. Harris Jr, *Molecular beam epitaxial GaAs heteroface solar cell grown on Ge.* Applied Physics Letters, 1980. **37**(12): p. 1104-1106.
7. Hudait, M., et al., *Comparative studies of Si-doped n-type MOVPE GaAs on Ge and GaAs substrates.* Materials Science and Engineering: B, 1998. **55**(1-2): p. 53-67.
8. Quezada, A.N., et al., *Critical thickness of Ge/GaAs (001) epitaxial films.* Superficies y vacío, 2003. **16**(4): p. 42-44.
9. Ting, S. and E. Fitzgerald, *Metal-organic chemical vapor deposition of single domain GaAs on Ge/Ge x Si 1− x/Si and Ge substrates.* Journal of Applied Physics, 2000. **87**(5): p. 2618-2628.
10. Yamaguchi, M. and C. Amano, *Efficiency calculations of thin-film GaAs solar cells on Si substrates.* Journal of applied physics, 1985. **58**(9): p. 3601-3606.
11. Groenert, M.E., et al., *Monolithic integration of room-temperature cw GaAs/AlGaAs lasers on Si substrates via relaxed graded GeSi buffer layers.* Journal of Applied Physics, 2003. **93**(1): p. 362-367.
12. Kuo, W.-C., et al., *High quality gaas epilayers grown on Si substrate using 100 nm Ge buffer layer.* International Journal of Photoenergy, 2016. **2016**.
13. Kamath, G., J. Ewan, and R. Knechtli, *Large-area high-efficiency (AlGa) As—GaAs solar cells.* IEEE Transactions on Electron Devices, 1977. **24**(4): p. 473-475.
14. Konagai, M., M. Sugimoto, and K. Takahashi, *High efficiency GaAs thin film solar cells by peeled film technology.* Journal of crystal growth, 1978. **45**: p. 277-280.

15. Yablonovitch, E., et al., *Extreme selectivity in the lift-off of epitaxial GaAs films.* Applied Physics Letters, 1987. **51**(26): p. 2222-2224.
16. Schermer, J., et al., *Epitaxial Lift-Off for large area thin film III/V devices.* physica status solidi (a), 2005. **202**(4): p. 501-508.
17. Tatavarti, R., et al. *Lightweight, low cost GaAs solar cells on 4 "epitaxial liftoff (ELO) wafers*. in *2008 33rd IEEE Photovoltaic Specialists Conference*. 2008. IEEE.
18. Van Geelen, A., et al., *Epitaxial lift-off GaAs solar cell from a reusable GaAs substrate.* Materials Science and Engineering: B, 1997. **45**(1-3): p. 162-171.
19. Schermer, J., et al., *High rate epitaxial lift-off of InGaP films from GaAs substrates.* Applied Physics Letters, 2000. **76**(15): p. 2131-2133.
20. Kayes, B.M., et al. *27.6% conversion efficiency, a new record for single-junction solar cells under 1 sun illumination*. in *2011 37th IEEE Photovoltaic Specialists Conference*. 2011. IEEE.
21. Choi, W., et al., *A Repeatable Epitaxial Lift-Off Process from a Single GaAs Substrate for Low-Cost and High-Efficiency III-V Solar Cells.* Advanced Energy Materials, 2014. **4**(16): p. 1400589.
22. Kayes, B.M., et al., *Flexible thin-film tandem solar cells with> 30% efficiency.* IEEE Journal of Photovoltaics, 2014. **4**(2): p. 729-733.
23. Horng, R.-H., et al. *High separation rate of epitaxial lift-off using hydrophilic solvent for III–V solar cell and reusable applications*. in *2015 IEEE 42nd Photovoltaic Specialist Conference (PVSC)*. 2015. IEEE.
24. Bauhuis, G., et al. *Substrate reuse for epitaxial lift-off of III-V solar cells*. in *Proceedings of the 22nd European Photovoltaic Solar Energy Conference: Milan*. 2007.
25. Selvamanickam, V., et al., *Germanium films with strong in-plane and out-of-plane texture on flexible, randomly textured metal substrates.* Journal of Crystal Growth, 2009. **311**(21): p. 4553-4557.
26. Dutta, P., et al., *High mobility single-crystalline-like GaAs thin films on inexpensive flexible metal substrates by metal-organic chemical vapor deposition.* Applied Physics Letters, 2014. **105**(9): p. 092104.
27. Rathi, M., et al., *High opto-electronic quality n-type single-crystalline-like GaAs thin films on flexible metal substrates.* Journal of Materials Chemistry C, 2017. **5**(31): p. 7919-7926.
28. Khatiwada, D., et al., *Passivation Studies On Single Junction GaAs Thin Film Solar Cells On Flexible Metal Tapes For Low Cost Photovoltaics.* ACS Applied Energy Materials, 2019.
29. Dutta, P., et al., *Flexible GaAs solar cells on roll-to-roll processed epitaxial Ge films on metal foils: a route towards low-cost and high-performance III–V photovoltaics.* Energy & Environmental Science, 2019. **12**(2): p. 756-766.
30. Ward, B., J.A. Notte, and N. Economou, *Helium ion microscope: A new tool for nanoscale microscopy and metrology.* Journal of Vacuum Science & Technology B: Microelectronics and Nanometer Structures Processing, Measurement, and Phenomena, 2006. **24**(6): p. 2871-2874.
31. Notte, J., et al., *An Introduction to Helium ion microscopy.* Microscopy and Microanalysis, 2006. **12**(S02): p. 126-127.
32. Joy, D.C. and B.J. Griffin, *Orion NanoFab-2nd Generation Helium Ion Microscope.* Microscopy and Microanalysis, 2013. **19**(S2): p. 854-855.

33. Wang, R., et al., *High mobility single-crystalline-like germanium thin films on flexible, inexpensive substrates.* Thin Solid Films, 2013. **527**: p. 9-15.
34. Selvamanickam, V., et al. *Novel, single-crystalline-like templates on low-cost, flexible substrates for high efficiency photovoltaics*. in *2010 35th IEEE Photovoltaic Specialists Conference*. 2010. IEEE.
35. Fischer, R., et al., *Dislocation reduction in epitaxial GaAs on Si (100).* Applied physics letters, 1986. **48**(18): p. 1223-1225.
36. Osbourn, G., *Strained-layer superlattices-A brief review.* IEEE journal of quantum electronics, 1986. **22**: p. 1677-1681.